INQUA Focus Group Earthquake Geology and Seismic Hazards

paleoseismicity.org

Shallow slip and fault geometry of the 2010 El Mayor-Cucapah (Mexico) earthquake from differential lidar

Lajoie, Lia (1), Johnson, Kendra (2), Nissen, Edwin (3)

(1) Department of Geophysics, Colorado School of Mines, 1500 Illinois St, Golden, CO 80401, USA, llajoie@mines.edu
(2) Global Earthquake Model, Via Ferrata 1, 27100 Pavia, Italy
(3) School of Earth and Ocean Sciences, University of Victoria, Victoria, B.C., V8P 5C2, Canada, enissen@uvic.ca

Abstract: *We investigate shallow slip in the 2010 M_w 7.2 El Mayor-Cucapah (Mexico) earthquake using three-dimensional surface deformation computed from pre- and post-event airborne light detection and ranging (lidar) topography (Glennie et al., 2014). By profiling the displacement field at densely-sampled (~300 m) intervals along the multi-segment rupture, and computing fault offsets in the E-W, N-S and vertical components, we map out the surface slip vector distribution. A principal goal is to resolve the discrepancy between field observations that are interpreted to reflect widespread low angle normal slip, and geodetic and/or seismological models which support rupture of sub-vertical faults. Since the computed slip vectors must lie in the plane of the fault, whose strike is known, we can calculate the dip (and rake) of the fault along strike and thus test these models explicitly. Along most of the fault trace, we find that coseismic faulting is steeply-dipping. However, a short (~5 km) section of the Paso Superior fault hints at local reactivation of a low-angle (<30°) structure.*

Keywords*: high resolution topography, differential lidar, earthquake deformation, low angle detachment faulting*

INTRODUCTION

We investigate fault zone surface deformation and subsurface fault geometry of the 4 April 2010 M_w 7.2 El Mayor-Cucapah earthquake in northern Baja California, Mexico (Figure 1). This earthquake incorporated several discrete dextral and dextral-normal faults with differing structural characteristics and ruptured through a variety of surface lithologies, enabling us to investigate the factors that control the surface expression of fault slip. It is also characterized by an exceptional wealth of field data and airborne and satellite imagery, providing new perspectives on the shallow slip in a large earthquake (e.g. Wei et al., 2011; Oskin et al., 2012; Gold et al., 2013; Fletcher et al., 2014, 2016; Barišin et al., 2015; Teran et al., 2015).

We build on earlier work by Glennie *et al*. (2014) by analyzing three-dimensional (3-D) coseismic surface displacements computed from pre- and post-earthquake airborne lidar topography. Discord between fault offsets surveyed in the field (Fletcher et al., 2014; Teran et al., 2015) and those determined over larger apertures using remote sensing data may reflect distributed strain within the fault zone and/or a shallow slip deficit (e.g. Dolan & Haravitch, 2014; Nissen et al., 2014). However, high-resolution surface deformation fields from modern airborne or satellite imagery also provide the means to produce much denser fault offset datasets than fieldwork would normally permit (e.g. Milliner et al., 2015).

Moreover, 3-D surface displacements mapped with differential lidar provide a unique opportunity to test for the involvement within the El Mayor-Cucapah earthquake of a low-angle (~20°-dipping) detachment fault. Normal slip on gently-dipping fault planes is mechanically unfavourable (e.g. Anderson 1905, 1951; Jackson & White, 1995), yet field observations in the northern rupture zone have been interpreted as indicating widespread oblique normal slip on a low-angle detachment underlying the Sierra Cucapah (Fletcher et al., 2014; Teran et al., 2015). However, this interpretation is inconsistent with several independent earthquake source models based on space

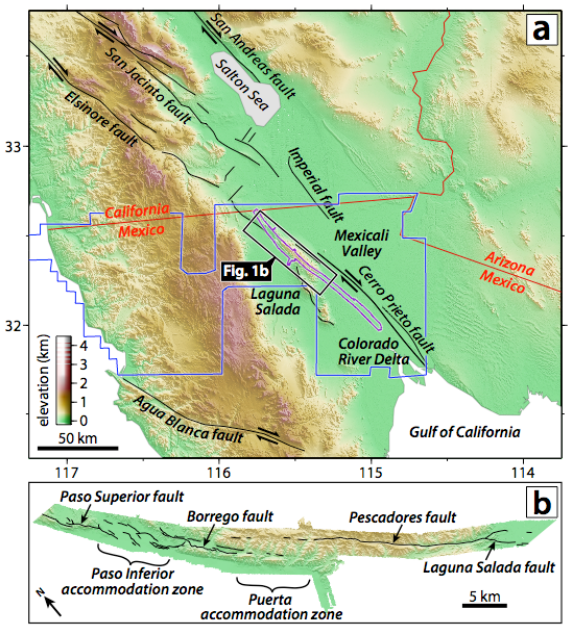

Figure 1: (a) Tectonic setting of the El Mayor-Cucapah earthquake showing other prominent regional faults. (b) The northern Sierra Cucapah section showing principal surface ruptures from Fletcher et al. (2014) plotted on post-earthquake lidar topography.

geodesy and/or seismology which all support steeply-dipping faulting (Fialko et al., 2010; Hauksson et al., 2011; Wei et al., 2011; Zheng et al., 2012; Uchide et al., 2013; Huang et al., 2017; Kyriakopoulos et al., 2017). A primary motivation of this study is to resolve this discrepancy.

DATA

The pre-event lidar data belong to a regional survey by the Instituto Nacional de Estadistica y Geografia (INEGI) in August 2006 (Figure 1a) and have an average density of ~0.013 points/m^2. The post-event data were collected by the National Center for Airborne Laser Mapping (NCALM) in August 2010, four months after the earthquake. They are much higher density, averaging ~10 points/m^2, but cover a relatively narrow ~3-5 km-wide swath centered on the surface rupture. This pair of datasets was first analyzed by Oskin et al. (2012) who mapped coseismic elevation changes by subtracting pre-event from post-event gridded digital terrain models (DTMs). However, this strategy does not account for lateral displacements and so cannot fully characterize the surface deformation field. Elevation changes are also of limited value in parts of the rupture zone containing rugged topography and where horizontal motions exceed vertical ones (e.g. Clark et al., 2017).

We instead used the 100 m-resolution 3-D surface deformation dataset of Glennie *et al.* (2014) (Figure 2) which was calculated by differencing pre- and post-event lidar point clouds using a windowed adaptation of the Iterative Closest Point (ICP) algorithm (Nissen et al., 2012, 2014). This has the advantage of capturing surface displacement vectors (as well as rotations) in each of the *x* (east-west), *y* (north-south) and *z* (vertical) dimensions. In practice there is too little relief within the Colorado River delta and Laguna Salada basin to resolve surface deformation in these areas, and initial results were also hampered by large N-S-trending artifacts related to errors in the pre-event survey data. Reprocessing of the pre-event lidar, described in Glennie et al. (2014), has reduced but not entirely eliminated these artifacts (Figure 2b, c).

METHODS

We developed a semi-automated procedure for measuring fault offsets from fault-perpendicular swath profiles through the *x*-, *y*-, and *z*-displacement fields. The swath profiles are centered at 300 m intervals along the fault surface trace (we use the published rupture map of Fletcher et al., 2014) and extend 1000 m orthogonally on either side of the fault. We use a swath width of 300 m, projecting all points within the swath onto the central profile line. Offsets are measured in each of the x, y and z displacement fields using straight-line, least-squares fits through the data points on each side of the fault, projecting to the fault, and computing the line separation at the fault (Milliner et al., 2015). In our implementation, the user cam define the limits for curve fitting on either side of the fault, allowing for some human discretion in removing artifacts and accounting for shorter-wavelength deformation.

The resulting *x*, *y* and *z* offsets at any point on the fault represent the local Cartesian slip vector; because this must lie in the plane of the fault, we can use knowledge of the local fault strike to compute the fault dip. Geometrically, this is done by projecting the slip vector onto a vertical plane orthogonal to the local fault strike and calculating its inclination. We also measure rake by taking the dot product of the strike and displacement vectors.

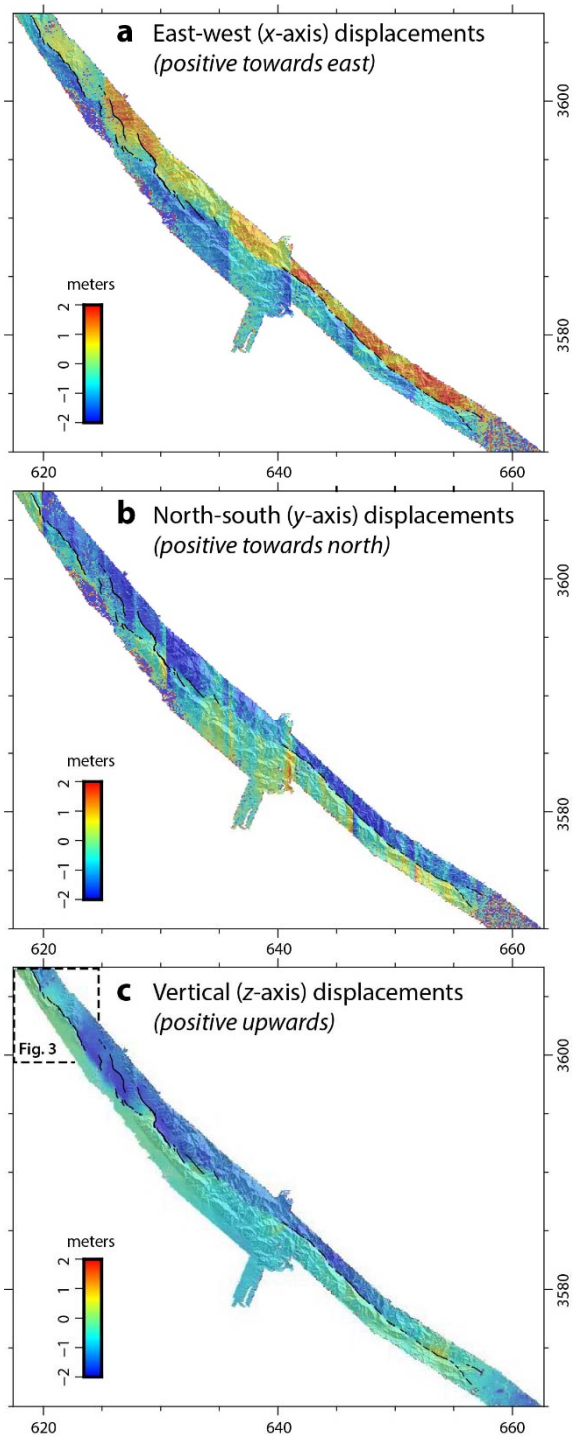

Figure 2: (a) East-west, (b) north-south and (c) vertical displacement field within the northern Sierra Cucapah section of the El Mayor-Cucapah rupture zone from application of our windowed adaptation to the Iterative Closest Point algorithm (Nissen et al., 2012, 2014; Glennie et al., 2014). Surface ruptures mapped in the field are shown by black lines (Fletcher et al., 2014; Teran et al., 2015). Coordinates are given in UTM Zone 11 kilometers.

RESULTS

To illustrate the type of data generated, Figure 3 shows profile locations and derived dip estimates along two segments of the Paso Superior fault in the northern rupture zone, plotted over the vertical displacement field (see Figure 2c for location). Figure 4 shows the same dip values, together with slip vector lengths (i.e. surface slip magnitudes), plotted as a function of distance along each fault segment. The Paso Superior fault is of particular interest as it encompasses some of the key field localities in which low-angle slip was observed on the ground (Fletcher et al., 2014; Teran et al., 2015).

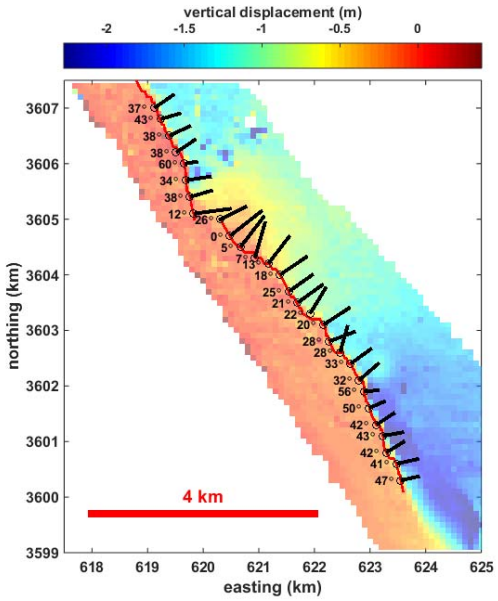

Figure 3: Calculated dip values for each profile location along the Paso Superior fault surface rupture (red line). Profile center points at 300 m intervals along the rupture are idicated by small circles. The black bars point down dip and are scaled by 90 - dip, such that longer arrows represent shallower dip angles. The background color map is the ICP vertical displacement field.

Along the southernmost Paso Superior fault, we estimate dip angles of 41° - 56°, reflecting the fact that fault throw is about equal to or slightly larger than heave. However, along the ~5 km middle part of the Paso Superior fault - close to the segment break - we calculate dips of 0° - 30°. These low angles can be confirmed visually from the raw displacement fields (Figure 2). The is only a faint discontinuity in the vertical displacement field at this location (reflecting small amounts of throw) but larger discontinuities in the horizontal displacement fields (reflecting larger amounts of heave). North of this central section, dips increase once again to values of ~40° at the northern edge of Figure 3.

Over a ~5 km section of the Paso Superior fault, the lidar data therefore support the field-based inferences of low-angle slip. Furthermore, the lidar displacement field hints that this slip extends over a distance of at least 2 km from the fault surface trace, and therefore probably several hundred meters into the subsurface. Existing seismological and geodetic models of the El Mayor-Cucapah earthquake therefore fail to capture important and genuine shallow-angle slip (Fialko et al., 2010; Hauksson et al., 2011; Wei et al., 2011; Zheng et al., 2012; Uchide et al., 2013; Huang et al., 2017; Kyriakopoulos et al., 2017). Instead, these models are likely to better characterize the deeper part of the fault zone, which is poorly sampled by the narrow (~3 km-wide) differential lidar footprint. We note that aftershock locations and mechanisms in this region appear inconsistent with deep slip on a NE-ward extension of the Paso Superior fault beneath the Mexicali Valley (Hauksson et al., 2011). We therefore envisage a scenario in which deep-seated slip on sub-vertical faulting transfers onto shallow, low-angle faulting only where no more favourably-oriented structure is available for reactivation.

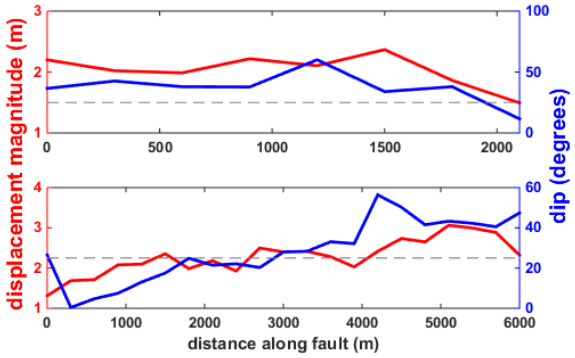

Figure 4: Surface slip magnitude (red) and fault dip (blue) calculated along strike for the northern (upper panel) and southern (lower panel) segments of the Paso Superior fault. Profiles are oriented N-S. Grey dashed lines delineate 25° dip.

This is further supported by the observed correlation between slip magnitude and fault dip along the Paso Superior fault, with correlation coefficients (R) of 0.57 for the northern segment (upper panel of Figure 4) and 0.64 for the southern segment (lower panel). Correlations for both fault segments are maximized at zero lag. This suggests that fault dip is providing a first-order control on displacement magnitude. For normal faults, with the maximum principal stress oriented vertically, Andersonian mechanics predicts optimally-oriented fault dip angles of ~60°; the less favorably-oriented the fault is, the less likely it is to slip (Anderson, 1905; Anderson 1951). The low-angle central Paso Superior fault appears to depress surface slip, whereas steeper sections of faulting to the north and south permit slip to break the surface relatively uninhibited.

CONCLUSIONS

Three-dimensional surface displacements in the 2010 El Mayor-Cucapah earthquake from differential lidar help resolve discrepancies between published fault models based on field measurements and those based on seismology and/or satellite geodesy. We do observe subsurface low-angle (0° - 30°) normal slip on a ~5 km section of the Paso Superior fault, consistent with local field measurements, but it is not pervasive throughout the wider Sierra Cucapah region as has been suggested. Furthermore, slip on the low-angle structure is depressed relative to adjacent, steeper sections of faulting.

Acknowledgements: We are grateful to all of the mapping and funding agencies involved in collecting and making available the lidar data. The Instituto Nacional de Estadistica y Geografia (INEGI) flew the pre-event survey, the National Center for Airborne Laser Mapping (NCALM) flew the post-earthquake survey, and the Open Topography facility (sponsored through NSF awards 1226353 and 1225810) curates both datasets. This research was supported primarily by the U.S. Geological Survey (USGS) through award G12AC20042, though we also acknowledge related support from the Southern California Earthquake Center (SCEC 14101) and the National Science Foundation (EAR 1461574). We thank Ramon Arrowsmith, Adrian Borsa, Alejandro Hinojosa Corona, Craig Glennie, Aravindhan Krishnan, Mike Oskin, and Sri Saripalli for many discussions of this work.

REFERENCES

Anderson, E.M., 1905. The Dynamics of Faulting. *Trans. Edinburch Geol. Soc*. 8 (3), 387-402.

Anderson, E.M., 1951. *The Dynamics of Faulting and Dyke Formation With Application to Britain*. 2nd ed., 206 pp., Oliver and Boyd, Edinburgh.

Barišin, I., Hinojosa-Corona, A., & Parsons, B., 2015. Co-seismic vertical displacements from a single post-seismic lidar DEM: example from the 2010 El Mayor-Cucapah earthquake. *Geophys. J. Int.* 202 (1), 328-346.

Clark, K.J., Nissen, E.K., Howarth, J.D., Hamling, I.J., Mountjoy, J.J., Ries, W.F., Jones, K., Goldstien, S., Cochran, U.A., Villamor, P., Hreinsdóttir, S., Litchfield, N.J., Mueller, C., Berryman, K.R., & Strong, D.T., 2017. Highly variable coastal deformation in the 2016 M_w 7.8 Kaikōura earthquake reflects rupture complexity along a transpressional plate boundary. *Earth Planet. Sci. Lett.* 474, 334-344.

Dolan, J.F., & Haravitch, B.D., 2014. How well do surface slip measurements track slip at depth in large strike-slip earthquakes? The importance of fault structural maturity in controlling on-fault slip versus off-fault surface deformation. *Earth Planet. Sci. Lett.* 388, 38-47.

Fialko, Y., Gonzalez, A., Gonzalez-Garcia, J.J., Barbot, S., Leprince, S., Sandwell, D.T., & Agnew, D.C., 2010. Static Rupture Model of the 2010 M7.2 El Mayor-Cucapah Earthquake from ALOS, ENVISAT, SPOT and GPS Data. *AGU Fall Meeting Abstr.*, T53B-2125.

Fletcher, J.M., Teran, O.J., Rockwell, T.K., Oskin, M.E., Hudnut, K.W., Mueller, K.J., Spelz, R.M., Akciz, S.O., Masana, E., Faneros, G., Fielding, E.J., Leprince, S., Morelan, A.E., Stock, J., Lynch, D.K., Elliott, A.J., Gold, P., Liu-Zeng, J., Gonzalez-Ortega, A., Hinojosa-Corona, A., & Gonzalez-Garcia, J., 2014. Assembly of a large earthquake from a complex fault system: Surface rupture kinematics of the 4 April 2010 El Mayor-Cucapah (Mexico) M_w 7.2 earthquake. *Geosphere* 10 (4), 797-827.

Fletcher, J.M., Oskin, M.E., & Teran, O.J., 2016. The role of a keystone fault in triggering the complex El Mayor-Cucapah earthquake rupture. *Nat. Geosci*. 9 (4), 303-307.

Glennie, C.L., Hinojosa-Corona, A., Nissen, E., Kusari, A., Oskin, M.E., Arrowsmith, J.R., & Borsa, A., 2014. Optimization of legacy lidar data sets for measuring near-field earthquake displacements. *Geophys. Res. Lett*. 41, 3494-3501.

Gold, P.O., Oskin, M.E., Elliott, A.J., Hinojosa-Corona, A., Taylor, M.H., Kreylos, O., & Cowgill, E., 2013. Coseismic slip variation assessed from terrestrial LiDAR scans of the El Mayor-Cucapah surface rupture. *Earth Planet. Sci. Lett.* 366, 151-162.

Hauksson, E., Stock, J., Hutton, K., Yang, W., Vidal-Villegas, J.A., & Kanamori, H., 2011. The 2010 M_w 7.2 El Mayor-Cucapah Earthquake Sequence, Baja California, Mexico and Southernmost California, USA: Active Seismotectonics along the Mexican Pacific Margin. *Pure. Appl. Geophys*. 168, 1255-1277.

Huang, M.H., Fielding, E.J., Dickinson, H., Sun, J., Gonzalez-Ortega, J.A., Freed, A.M., & Bürgmann, R., 2017. Fault geometry inversion and slip distribution of the 2010 M_w 7.2 El Mayor-Cucapah earthquake from geodetic data. *J. Geophys. Res.* 122, 607-621.

Jackson, J.A., & White, N.J., 1989. Normal faulting in the upper continental crust: observations from regions of active extension, *J. Struct. Geol.* 11, 15-36.

Kyriakopoulos, C., Oglesby, D.D., Funning, G.J., & Ryan, K.J., 2017. Dynamic Rupture Modeling of the *M*7. 2 2010 El Mayor-Cucapah Earthquake: Comparison With a Geodetic Model. *Journal of Geophysical Research: Solid Earth* 122 (12), 10263-10279.

Milliner, C.W.D., Dolan, J.F., Hollingsworth, J., Leprince, S., Ayoub, F., & Sammis, C., 2015. Quantifying near-field and off-fault deformation patterns of the 1992 M_w 7.3 Landers earthquake. *Geochem. Geophys. Geosyst*. 16, 1577-1598.

Nissen, E., Krishnan, A.K., Arrowsmith, J.R., & Saripalli, S., 2012. Three-dimensional surface displacements and rotations from differencing pre- and post-earthquake LiDAR point clouds. *Geophys. Res. Lett*. 39, L16301.

Nissen, E., Maruyama, T., Arrowsmith, J.R., Elliott, J.R., Krishnan, A.K., Oskin, M.E., & Saripalli, S., 2014. Coseismic fault zone deformation revealed with differential lidar: Examples from Japanese $M_w \sim 7$ intraplate earthquakes. *Earth Planet. Sci. Lett.* 405, 244-256.

Oskin, M.E., Arrowsmith, J.R., Corona, A.H., Elliott, A.J., Fletcher, J.M., Fielding, E.J., Gold, P.O., Garcia, J.J.G., Hudnut, K.W., Liu-Zeng, J., & Teran, O.J., 2012. Near-Field Deformation from the El Mayor-Cucapah Earthquake Revealed by Differential LIDAR. *Science* 335, 702-705.

Teran, O., Fletcher, J.M., Oskin, M.E., Rockwell, T.K., Hudnut, K.W., Spelz, R.M., Akciz, S.O., Hernandez-Flores, A.P., & Morelan, A.E., 2015. Geologic and structural controls on rupture zone fabric: A field-based study of the 2010 M_w 7.2 El Mayor-Cucapah earthquake surface rupture. *Geosphere* 11 (3), 899-920.

Uchide, T., Yao, H., & Shearer, P.M., 2013. Spatio-temporal distribution of fault slip and high-frequency radiation of the 2010 El Mayor-Cucapah, Mexico earthquake. *J. Geophys. Res*. 118, 1546-1555.

Wei, S., Fielding, E., Leprince, S., Sladen, A., Avouac, J.-P., Helmberger, D., Hauksson, E., Chu, R., Simons, M., Hudnut, K., Herring, T., & Briggs, R., 2011. Superficial simplicity of the 2010 El Mayor-Cucapah earthquake of Baja California in Mexico. *Nat. Geosci*. 4, 615-618.

Zheng, Y., Li, J., Xie, Z., & Ritzwoller, M.H., 2012. 5Hz GPS seismology of the El Mayor-Cucapah earthquake: estimating the earthquake focal mechanism. *Geophys. J. Int*. 190, 1723-1732.